Inclusion parameters estimation using INBEM and CNNs with gradient-based feature extraction⋆

Roman Havdulskyi [1,*,†], Liubov Zhuravchak[1,†] and Vitaliy Yakovyna [2,†]

[1] *Lviv Polytechnic National University, S. Bandera Street 12, 79013 Lviv, Ukraine*
[2] *University of Warmia and Mazury in Olsztyn, Oczapowskiego Street 2, 10-719 Olsztyn, Poland*

Abstract

The presence of foreign inclusions in physical objects may affect their physical properties. Existing research employs different techniques, but all of them rely on data that can be obtained either by conducting a real-world experiment or employing numerical methods. Both options are quite time-consuming and resource-consuming. This study aims to propose a more optimal way to approach estimating both geometric and conductivity parameters using a more resource-efficient numerical method called the indirect near boundary method (INBEM). Using INBEM to generate the dataset makes it possible to consider a wider variety of objects and inclusion parameters. As more data is available, deeper research into preprocessing techniques and neural network models is becoming feasible. Thus, several CNN architectures and preprocessing methods were evaluated. The proposed preprocessing method improved geometric parameters prediction by up to 4 times compared to just normalization. The best-performing model (CNN3-FD 2nd-order) achieved a mean absolute error close to 0.01. Thus, combining INBEM with CNNs and proposed preprocessing techniques proves to be an efficient method of inclusion localization. It established ground for future research aimed at detecting several inclusions at once and fine-tuning INBEM to increase accuracy in real-world experiments.

Keywords

Neural networks, inclusion recognition, stationary process, convolution neural network, machine learning, non-destructive testing, potential theory, computational experiment.

1. Introduction

The presence of inclusions in physical objects has an impact on their properties and behavior. Thus, detection and identification of them is an essential task to be researched. From a mathematical perspective, such problems belong to the class of inverse problems, particularly in the modeling of stationary processes, and are part of potential theory in inhomogeneous objects.

Most studies focus on detecting defects in objects of clearly defined size [1, 2]. Developing models capable of recognizing inclusions in objects of varying sizes or even different shapes is much less common. Most of the recent studies focus on defects localization in an object [1, 3, 4], rarely on defects or media characterization [6]. The media's conductivity parameter estimation is not as well researched as geometric parameters estimation.

To detect and localize defects, architectures like CNN or its descendants are often employed. Despite following quite similar ideas, the researchers employ different combinations of feature extraction methods or modifications of state-of-the-art models [6, 7]. A combination of GAN methods [3, 8] with deep neural networks is enabled as an alternative way to improve performance.

Despite having all the powerful tools employed, there is a persistent problem of building quite a large dataset with a wide variety of features. Data obtained during real-world experiments is highly

ICyberPhyS'25: 2nd International Workshop on Intelligent & CyberPhysical Systems, July 04, 2025, Khmelnytskyi, Ukraine
[1*] Corresponding author.
[†] These authors contributed equally.
roman.i.havdulskyi@lpnu.ua (R. Havdulskyi); liubov.m.zhuravchak@lpnu.ua (L. Zhuravchak); yakovyna@matman.uwm.edu.pl (V. Yakovyna)
0009-0004-6737-6018 (R. Havdulskyi); 0000-0002-1444-5882 (L. Zhuravchak); 0000-0003-0133-8591 (V. Yakovyna)

valuable, but it is costly in terms of money and time to obtain. Using numerical methods, such as FEM [1], partially resolves the issue. However, such techniques require quite a lot of computational resources.

This paper proposes employing an indirect near-boundary element method [9] (INBEM) to generate the dataset. A model to estimate both geometric and conductivity parameters is proposed. A combination of feature extraction methods is proposed and tested out as well. As described in advance, conductivity estimation highly relies on accurate geometric parameters estimation. This paper mainly focuses on estimating geometric parameters as a key to approach accurate conductivity estimation.

The object of the research is the recognition of the physical and geometric characteristics of a foreign inclusion.

The subject of the research is neural network methods and tools for recognizing the characteristics of an inclusion.

The purpose of the research is to analyze methods and tools for recognizing the physical and geometric characteristics of a foreign inclusion.

The research novelty is combining neural networks with an efficient numerical method (the indirect near boundary element method) for solving inverse problems of potential theory.

2. Related works

In paper [1] finite element simulation is employed to generate synthetic data. To augment data brightness, contrast, exposure and noise adjustments were employed. To preprocess data Sobel, Prewitt and Roberts operators were enabled. Transfer learning was considered to fine-tune state of art models.

The research [2] aims to recognize defects with different sizes and depth of placement. It employs both real-world experiments and FEM simulation to generate synthetic data. The defect was considered as holes with circles of different diameters and depths. To preprocess data, polynomials and Padé approximation were employed. The proposed method enables using LSTM architecture.

In paper [3] IRT-GAN architecture was proposed to detect defects. The architecture uses U-Net as a generator and PatchGAN with GlobalGAN as a discriminator to improve segmentation accuracy. To improve noise suppression, Spatial Group-wise Enhance Layer is employed. The dataset was obtained by numerical experiment. To improve model generalization data augmentation is employed by altering image rotation, scale and noise level.

The research [4] proposed a method that consists of data compression to reduce data size by employing Newton's Cooling Law. Background removal is done by local thresholding and Canny edge detection. Defect detection is achieved by computing thermal contrasts, maximum amplitude and time constants. A change in heat flow direction is considered to improve precise defect localization.

In research [5], a real-world experiment was conducted. Thermal feature extraction is done by considering thermal amplitude, time constant and thermal constant. Defect edge highlighting is done by computing derivative and processing it using Canny edge detection, applied thresholding before. Thermal features were mapped into an RGB image to make defect visualization clearer.

The paper [6] considers such defects as flat-bottom holes and Teflon inserts in plexiglass, carbon fiber reinforcement polymer and steel. An experiment was conducted to build a dataset. Data augmentation was employed too. This paper proposes using PCT (Principal Component Thermography) to extract features. It uses YOLOv3 and Faster-RCNN to detect defects. U-Net and Res-U-Net were employed for semantic segmentation. Instance segmentation is done by Mask-RCNN and Center-Mask.

In paper [7], the proposed method uses Principal Component Analysis (PCA) to enhance defect features, deep convolutional neural networks with Region of Interest (ROI) to extract features and Faster-RCNN to detect objects. The dataset was built by conducting a real-world experiment. Both PCA and data augmentation were employed.

The paper [8] aims to address the limitations of PCT. It proposes using generative artificial neural networks (GANs) to enhance data. The proposed method employs using GAN before applying PCT. Specifically, it employs Spectral Normalized GAN and Convolutional Autoencoder. The real-world experiment was conducted to scan panel painting with artificially induced defects.

In paper [10], an adaptive wavelet neural network is employed to detect defects by using a two-step approach: it reconstructs the 3D point cloud, then it enhances the defect area. As a result, the proposed approach outperforms traditional Terrestrial Laser Scanners (TLS) based crack detection.

The paper [11], contrary to other papers, focused on crack detection based on photos of concrete objects. The dataset consists of 990 RGB images. It proposed an approach of using transfer learning. It estimated the performance of a few well-known models, such as ResNet18, GoogLeNet, MobileNetV2 and VGG16. The best performance was shown by ResNet18.

A method of continuous laser-based active thermography was proposed in the paper [12]. A real-world experiment was conducted. Except for the experimental tools, it proposes using thermal sequence processing by pixel-wise averaging. It states that Roberts filtering performed better than the others.

The research [13] aims to use infrared thermography to monitor delicate cultural heritage objects. The preprocessing is done by contrast enhancement and noise reduction. It proposes using Mask R-CNN to detect defects.

In paper [14], improved Faster-RCNN is employed for crack detection. It uses VGG-16 as its backbone by employing transfer learning. The dataset was built by conducting a real-world experiment. It consists of 3125 infrared thermal images of steel plates.

In paper [15], machine learning algorithms, such as linear regression, multilayer perceptron and a few more, were compared to characterize internal defects in additive materials. The features considered by the models were conductivity coefficient, max heating temperature, front contrast, rear contrast and other physical parameters.

The paper [16] employs hybrid CNN in combination with a physically informed neural network (PINN) to reconstruct temperature distribution for 3D thermal tomography. The finding of the paper is that using standard CNNs fails to reconstruct a distribution under real-world noise. Besides that, a combination of CNN with PINN achieved the best result in processing noisy data.

3. Solving the direct problem of potential theory for a piecewise-homogeneous body

Before developing an approach to solving the inverse problem, it is necessary to obtain a series of datasets corresponding to the solutions of the direct problem with varying geometric and physical characteristics of the inclusion. The mathematical models of steady-state processes, constructed for methods based on the use of natural and artificial potential fields (gravitational, magnetic, electric, thermal, filtration) to detect inhomogeneities within an object, consist of Laplace equations:

$$\boldsymbol{P}_0^{(m)}(u^{(m)}(x)) = \Delta u^{(m)}(x) = 0,\ x \in \Omega_m, \Omega_m \subset \boldsymbol{R}^2, m = 0,1, \tag{1}$$

supplemented with prescribed boundary conditions:

$$u^{(0)}(x) = f_\Gamma^{(1)}(x),\ x \in \partial\Omega^{(1)}, \frac{\partial u^{(0)}(x)}{\partial \boldsymbol{n}^{(0)}(x)} = f_\Gamma^{(2)}(x),\ x \in \partial\Omega^{(2)}, \tag{2}$$

and ideal contact conditions at the interfaces between media:

$$u^{(0)}(x) = u^{(1)}(x), \lambda_0 \frac{\partial u^{(0)}(x)}{\partial \boldsymbol{n}^{(0)}(x)} = -\lambda_1 \frac{\partial u^{(1)}(x)}{\partial \boldsymbol{n}^{(1)}(x)}, x \in \partial\Omega_1. \tag{3}$$

Here Ω_m is a homogeneous domain with a constant physical property λ_m (conductivity); $\boldsymbol{n}^{(0)}(x) = (\boldsymbol{n}_1^{(0)}(x), \boldsymbol{n}_2^{(0)}(x))$ is the unit outward normal vector uniquely defined on the boundary $\partial\Omega_0$; $\Delta = \frac{\partial^2}{\partial x_1^2} + \frac{\partial^2}{\partial x_2^2}$ is the Laplace operator, x=(x_1, x_2), $\cup_{q=1}^2 \partial\Omega^{(q)} = \partial\Omega$; $\partial\Omega^{(1)} \cap \partial\Omega^{(2)} = \emptyset, \Omega =$

$\Omega_0 \cup \Omega_1 \cup \partial\Omega_1$, $\partial\Omega_1$ is the boundary of the inclusion Ω_1; and x_1, x_2 is the Cartesian coordinate system.

To solve the boundary value problem (1) – (3), the indirect near-boundary element method was used, which has demonstrated higher accuracy compared to the boundary element method (BEM), as well as lower requirements for the programmer's mathematical expertise [9, 17].

The external near-boundary regions are discretized into near-boundary elements (NBEs) G_v^m $(v = 1,\dots,V_m)$ and families of points $G_v^{mk}(k = 1,\dots,K_{mv})$ are introduced on them. For each G_v^m unknown functions $\varphi_v^{(m)}(x)$ are introduced, which describe the collective behavior of fictitious sources placed at the points G_v^{mk}.

Since for the Laplace operator $\boldsymbol{P}_0^{(m)}(u^{(m)}(x))$ the known fundamental solution (FS) $\breve{U}^{(m)}(x,\xi)$ exists, the integral representations of the solutions to equations (1) and their normal derivatives have the following form:

$$u^{(m)}(x) = \boldsymbol{F}^{(m)}(x,\breve{U}^{(m)}) + C_m, \qquad \partial u^{(m)}(x)/\partial \boldsymbol{n}^{(m)}(x) = \boldsymbol{F}^{(m)}(x,\breve{Q}^{(m)}), \tag{4}$$

where $\boldsymbol{F}^{(m)}(x,\Phi^{(m)}) = \sum_{v=1}^{V_m}\sum_{k=1}^{K_{mv}}\Phi^{(m)}(x,\xi^{v0k})\varphi_v^{(m)}(\xi^{v0k})$, $\breve{U}^{(m)}(x,\xi) = -\frac{1}{2\pi\lambda_m} ln\,|r/r_0|$,

$\breve{Q}^{(m)}(x,\xi) = \sum_{l=1}^{2}\breve{Q}_l^{(m)}(x,\xi)\boldsymbol{n}_l^{(m)}(x)$, $\breve{Q}_l^{(m)}(x,\xi) = -\frac{y_l}{2\pi r^2}$, |x| is the modulus of vector x, r_0 is a constant used to improve computational stability, $\xi = (\xi_1,\xi_2) \in \boldsymbol{R}^2$, $r^2 = \sum_{i=1}^{2} y_i^2$, $y_i = x_i - \xi_i$.

By directing x in equation (4) from the interior of the domain Ω toward its boundary $\partial\Omega$ to satisfy conditions (2) and (3), and by adding an equation expressing the condition that the total effect of all sources acting in $\boldsymbol{R}_m^2$ is zero, we obtain the boundary integral equations (BIE):

$$\boldsymbol{F}^{(0)}(x,\breve{U}^{(0)}) + C_0 = f_\Gamma^{(1)}(x), \quad x \in \partial\Omega^{(1)}, \qquad \boldsymbol{F}^{(0)}(x,\breve{Q}^{(0)}) = f_\Gamma^{(2)}(x), \quad x \in \partial\Omega^{(2)}, \tag{5}$$

$$\boldsymbol{F}^{(0)}(x,\breve{U}^{(0)}) + C_0 - \boldsymbol{F}^{(1)}(x,\breve{U}^{(1)}) - C_1 = 0, \qquad \lambda_0\boldsymbol{F}^{(0)}(x,\breve{Q}^{(0)}) + \lambda_1\boldsymbol{F}^{(1)}(x,\breve{Q}^{(1)}) = 0, \tag{6}$$

$$x \in \partial\Omega_1,$$

$$\boldsymbol{F}^{(m)}(x,1) = 0,\ x \in \boldsymbol{R}_m^2. \tag{7}$$

The boundary integral equations (5)–(7), after approximating the functions $\varphi_v^{(m)}(x)$ by unknown constants d_v^m, are written in the form of a system of linear algebraic equations (SLAE):

$$\begin{gathered}
\sum_{v=1}^{V_0}\breve{A}_v^0(x^{0w},\breve{U}^{(0)})d_v^0 + C_0 = f_\Gamma^{(1)}(x^{0w}),\ x^{0w} \in \partial\Omega^{(1)},\ w = 1,\dots,V_0^{(1)},\\
\sum_{v=1}^{V_0}\breve{A}_v^0(x^{0w},\breve{Q}^{(0)})d_v^0 = f_\Gamma^{(2)}(x^{0w}),\ x^{0w} \in \partial\Omega^{(2)},\ w = V_0^{(1)}+1,\dots,V_0^{(2)},\\
\sum_{v=1}^{V_0}\breve{A}_v^0(x^{1w},\breve{U}^{(0)})d_v^0 + C_0 - \sum_{v=1}^{V_1}\breve{A}_v^1(x^{1w},\breve{U}^{(1)})d_v^1 - C_1 = 0,\ x^{1w} \in \partial\Omega_1,\\
w = 1,\dots,V_1,\\
\lambda_0\sum_{v=1}^{V_0}\breve{A}_v^0(x^{1w},\breve{Q}^{(0)})d_v^0 + \lambda_1\sum_{v=1}^{V_1}\breve{A}_v^1(x^{1w},\breve{Q}^{(1)})d_v^1 = 0,\\
\sum_{v=1}^{V_m}\breve{A}_v^m(x,1)d_v^m = 0,\ x \in \mathbf{R}_m^2,
\end{gathered} \tag{8}$$

where $\breve{A}_v^{(m)}(x,\Phi^{(m)}) = \sum_{k=1}^{K_{mv}}\Phi^{(m)}(x,\xi^{v0k})$.

Having determined the unknowns d_v^m and C_m from (8), we use formulas analogous to (4) to compute the desired functions $u^{(m)}(x)$ and their normal derivatives at both internal points of each subdomain Ω_m, and at the interfaces between media, since the inclusions Ω_1 and the surrounding medium Ω_0 are now treated as completely independent regions [17]:

$$u^{(m)}(x^{mz}) = \sum_{v=1}^{V_m}\breve{A}_v^m(x^{mz},\breve{U}^{(m)})d_v^m + b^m(x^{mz},\breve{U}^{(m)}) + C_m,\ x^{mz} \in \boldsymbol{Z}_m, \tag{9}$$

$$\frac{\partial u^{(m)}(x^{mz})}{\partial \boldsymbol{n}^{(m)}(x)} = \sum_{v=1}^{V_m} \check{A}_v^m(x^{mz}, \check{Q}^{(m)}) d_v^m + b^m(x^{mz}, \check{Q}^{(m)}),$$

where $\boldsymbol{Z}_m$ is the set of observation points $x^{mz} \in \partial\Omega_m \cup \Omega_m$.

It is worth mentioning that the use of point families on NBEs made it possible, unlike in the BEM, to avoid prior analytical extraction of singularities (principal values) when computing the normal derivatives of the desired functions. Point families significantly simplify the problem-solving algorithm, as they replace integration over NBEs with the summation of products of the fundamental solution and the unknown (8) or known (9) source intensities. Thus, they can be recommended for obtaining initial approximations as a rapid method for solving inverse problems of mathematical physics, where time optimization is prioritized over accuracy.

4. Generating heat distribution data by indirect near boundary element method

To generate a dataset the INBEM [18] is employed. As already mentioned before, the main advantage of it is the significantly lower computation cost compared with BEM and similar methods. The visual representation of an object with inclusion is shown in Figure 1.

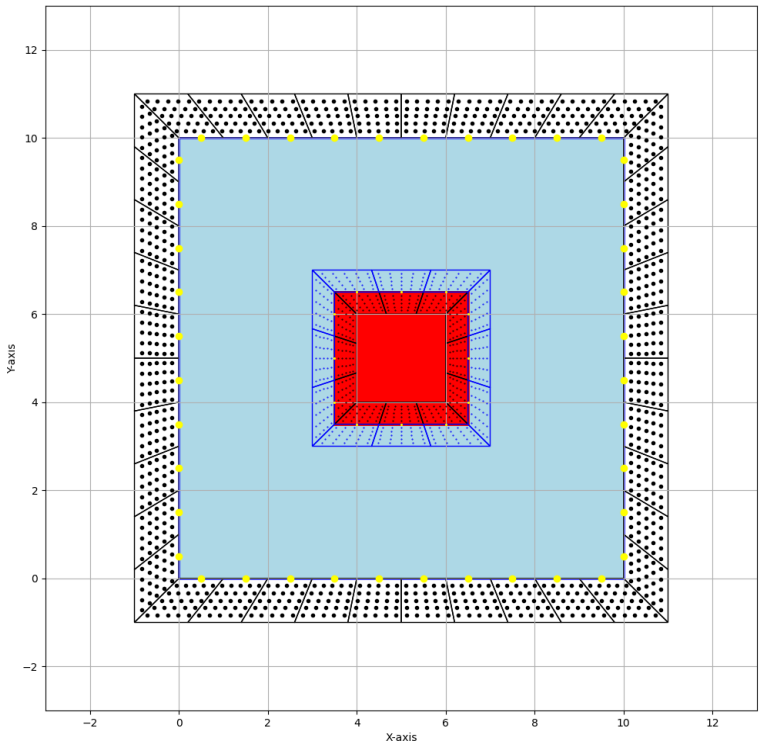

Figure 1: A visual representation of discretization of the near-boundary domain into near-boundary elements.

The boundary conditions are the following: upper and lower sides are thermally insulated, the left side is set as Dirichlet boundary condition of 0°C and the right side as Dirichlet boundary condition of 10°C. The thermal conductivity coefficient of the medium is set to $1\ \frac{W}{(m*K)}$. The temperature distribution within the object is shown in Figure 2.

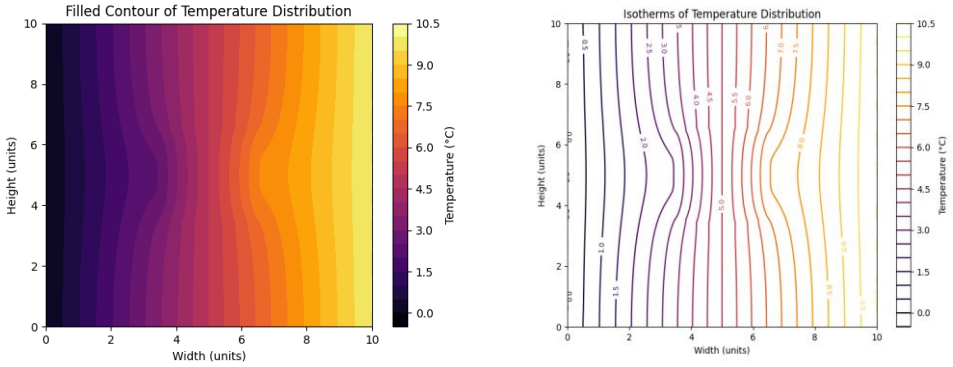

Figure 2: Visual representations of the temperature distribution using isothermal lines.

The dimension of the generated data is 100 * 100 to make both the dataset and model more generic. The object heat data is put at the very beginning of the distribution array. The rest is filled up with zeros as the padding.

In addition to temperature data, each dataset element includes information about the coordinates of the lower-left corner of the inclusion, its height, width, and thermal conductivity coefficient. The data is stored in JSON files, each of which represents information from a computational experiment with specific variable parameters. The dataset consists of 4 subsets described in detail in Table 1. To increase the variance of geometric parameters, the variability of the conductivity parameter is quite poor. The common parameters of the subsets are:

- thermal conductivity coefficient variability: 4.2, 5.9, 8.6, 12.9, 14.6;
- a number of fictitious point sources in each NBE: 5 rows, 5 columns, a total of 25;
- number of NBEs on the contact boundary: equal to the width/length of the inclusion;
- height of the NBE at the object's boundary: 1;
- height of the NBE at the contact boundary: 0.5.

Table 1
Subset parameters

Object width/ height	Inclusion width/height	X/Y coordinate	Number of NBEs	Total elements
10/10	1 to 8, step 0.5/ 1 to 8, step 0.5	0.6 to 8.1, step 0.5/ 0.6 to 8.1, step 0.5	10 per side, total 40	91,125
10/5	1 to 3, step 0.5/ 1 to 6, step 0.5	0.6 to 8.1, step 0.5/ 0.6 to 3.1, step 0.5	10 * 5, total 30	13,500
5/10	1 to 6, step 0.5/ 1 to 3, step 0.5	0.6 to 3.1, step 0.5/ 0.6 to 8.1, step 0.5	5 * 10, total 30	13,500
8/4	1 to 6, step 0.5/ 1 to 2, step 0.5	0.6 to 6.1, step 0.5/ 0.6 to 2.1, step 0.5	8 * 4, total 24	3,465

5. Feature extraction

To extract informative features from the heat distribution data gradient approximation and binarization are employed. All of them are aimed at detecting the edges of the inclusion. As the input data may contain paddings the representable part is extracted based on the object dimensions provided. Derivative approximation is considered as a basic method [19, 20]. To approximate derivatives the forward difference, a combination of forward, central, and backward differences were considered. As the heat distribution data is present as a 2D array then its derivative is calculated in the following way:

$$|\nabla T| = \sqrt{\left(\frac{\partial T}{\partial x}\right)^2 + \left(\frac{\partial T}{\partial y}\right)^2}. \quad (10)$$

The first-order derivative of the thermal data is calculated to highlight regions with abrupt temperature changes. These regions represent the boundaries of inclusions.

The forward difference method (FD) is enabled for the approximation of derivatives (10). It is calculated in the following way:

$$\frac{\partial T}{\partial x} \approx \frac{T(x + \triangle x) - T(x)}{\triangle x}. \quad (11)$$

Despite its being less accurate, this method can calculate derivatives at the edge, specifically for the first point. As this method decreases dimension by 1, the last element is padded by the appropriate element from the distribution. It leads to a spike around the last element, which can be seen visually as high-contrast lines by the end of each axis. Visual representations of objects of size 8x4 with inclusion are shown in Figure 3. For visualization purposes, an object with a dimension of 8*4 is taken as an example to prove correct data extraction.

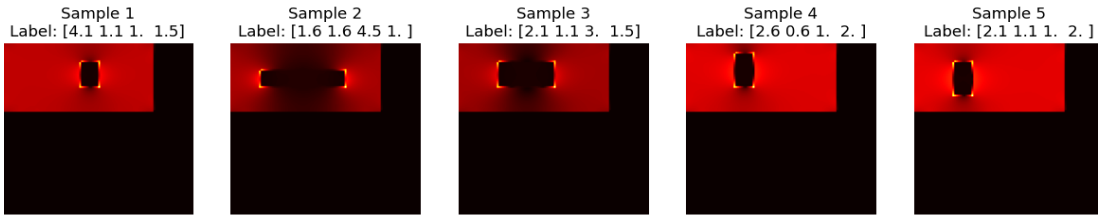

Figure 3: Visual representations of 1st-order derivative approximation by forward differences.

A combination of forward, central, and backward methods (CD) is taken to achieve a better quality of approximation. The formulas for calculating central and backward differences are the following:

$$\frac{\partial T}{\partial x} \approx \frac{T(x + \triangle x) - T(x - \triangle x)}{2 \triangle x}, \quad (12)$$

$$\frac{\partial T}{\partial x} \approx \frac{T(x) - T(x - \triangle x)}{\triangle x}. \quad (13)$$

The central difference method (12) is quite more accurate. However, it can't be applied to the edges. Thus, to resolve it, combinations of forward and backward differences are used at the edges. Visual representations of objects of size 8x4 with inclusion are shown in Figure 4.

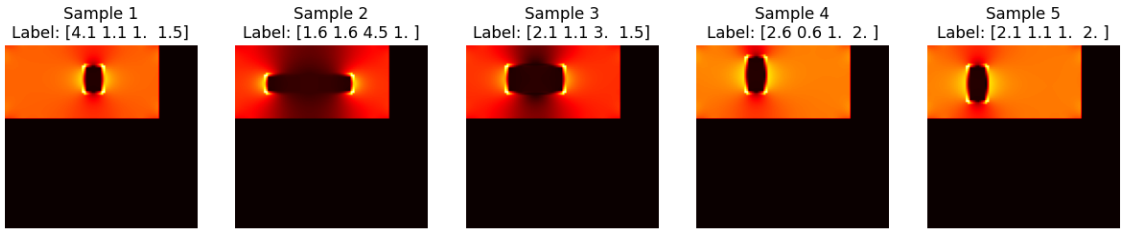

Figure 4: Visual representations of 1st-order derivative approximation by the combination of central (12), forward (11) and backward (13) differences.

As the second derivative represents acceleration in terms of heat distribution, it allows identifying clear corners and edges of the inclusion [19]. Of course, noise presence may be considered as parts of false edges or contours. However, we are not considering noise robustness in the scope of this work and it is the point for future research. A visual representation of the preprocessed thermal data using the forward difference method is shown in Figure 5. The red-highlighted areas likely represent

the contours of inclusions.

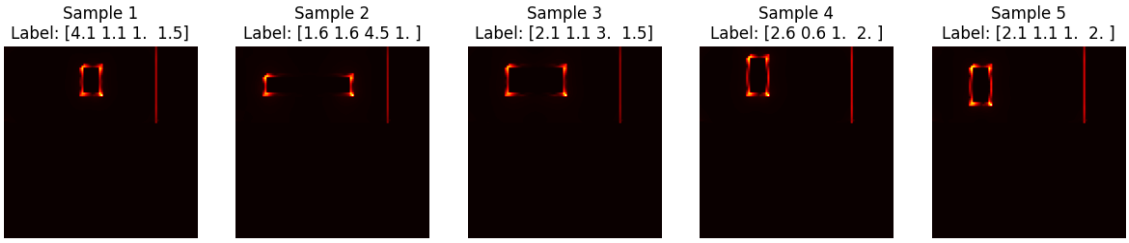

Figure 5: Visual representations of 2nd-order derivative approximation by forward differences.

Visual results of using a combination of forward, central and backward differences to approximate the second derivative are given in Figure 6.

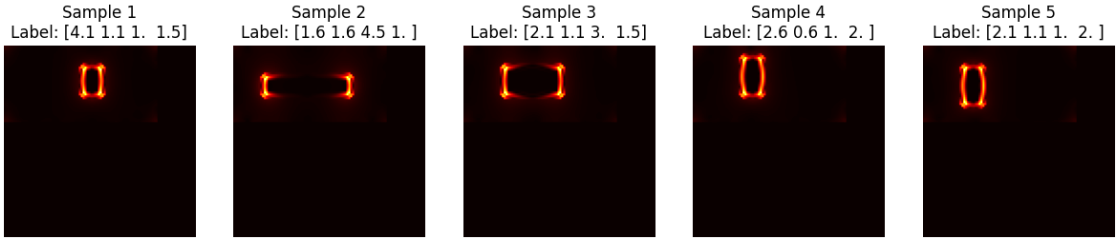

Figure 6: Visual representations of 2nd-order derivative approximation by the combination of central, forward and backward differences.

As shown in the previous figures, the contours are visually identifiable. However, there is a presence of peaks at the edges of the inclusion. Some parts of the contour are quite thick. The reason is partially lying in the lower accuracy of the INBEM on the corners. To resolve it, quite a fine-tuning is required to optimize accuracy at the corners; it is the point of the upcoming research.

Aiming to receive a strict contour of the inclusion, binarization is also employed. The threshold to choose between 1 and 0 is determined by taking the mean of the heat image distribution. Visualization is shown in Figure 7.

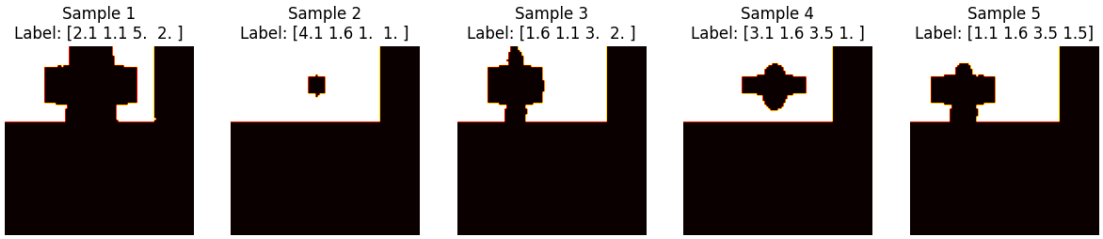

Figure 7: Visual representations of 2nd-order derivative approximation by a combination of central, forward and backward differences with binarization technique.

6. Method of estimating both geometric and conductivity parameters

The model of processing heat distribution data is visualized in Figure 8. As the input the model takes distribution data. Considering the input dimension as 100 * 100, to support objects with different sizes and shapes the model also requires dimension data. It is necessary to extract the object heat data and do not consider paddings as it might lead to less accurate estimation. Then the features are extracted using already described techniques. The next step involves a neural network model to predict the geometric parameters of the inclusion. This data is required to proceed with extracting conductivity features from the distribution. A neural network estimates conductivity. As a result, both geometric parameters and conductivity are estimated.

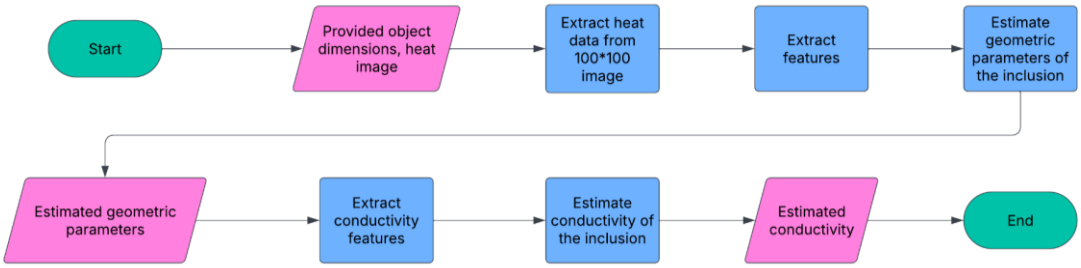

Figure 8: Diagram explaining the method of recognizing both geometric and conductivity parameters.

As is clearly shown, estimating conductivity relies on precise geometric data estimation. The main goal of this paper is to validate feature extraction techniques first as a tool to improve the precision of the neural network. At the same time, straight-forward neural network models are enabled to achieve the next goals:

- do not overfit the model, as the large one might just remember the data instead of generalizing it;
- start building the model from scratch, increasing complexity only when it is required as a complex one will also require more computational resources.

Despite the paper aiming to improve geometric parameters estimation, the method of conductivity estimation is provided in advance. The conductivity features extraction method consists of the following steps:

- identify a horizontal segment that runs along the entire object precisely through the center of the inclusion;
- determine the gradient at four points before the contact boundary and at four points beyond the contact boundary.

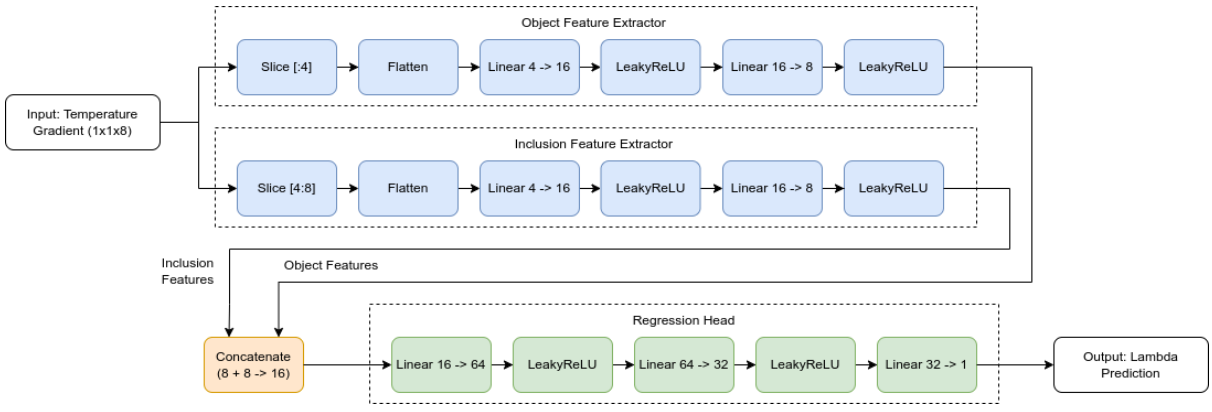

Figure 9: Visual representation of the conductivity extraction model.

The method reduces the data dimensionality to 1D and enables clearer extraction of a greater number of informative features. The neural model architecture for estimation inclusion conductivity is visualized in Fig. 9. We assume that the main object's conductivity is equal to 1 and do not accept it as an input parameter. In the future, object conductivity also must be considered. The proposed model includes three main stages:

- deep object and inclusion feature extraction from the already preprocessed data;
- concatenating features;

- conductivity parameters estimation based on concatenated features.

As of the early stage of the research, the inclusion detection problem is considered a simple regression task that predicts a bounding box for a single object. We neglect the fact that there might be no inclusion or more than one. This is the purpose of the upcoming research and will be resolved by enabling a bounding box or anchor-free methods to the model. For the research purpose CNNs [21] with several convolution layers from 1 to 3 were used. We call those models CNN1, CNN2, CNN3.

The CNN1 network consists of one convolutional layer followed by a pooling operation and two fully connected (dense) layers. The architecture is as follows:

- Input Layer: the model accepts a single-channel input image of size 100×100.
- Conv2D: 16 filters of size 3×3, a stride of 1 and padding of 1.
- Activation: ReLU.
- Max Pooling Layer.
- Flattening Layer.
- Fully Connected Layer.
- Activation: ReLU.
- Output Layer: 4 output values representing x, y, width, height.

The architecture of CNN2 is the following:

- Input Layer: the model accepts a single-channel image input of dimensions 100×100.
- Conv2D: 16 filters of size 3×3, a stride of 1, and padding of 1.
- Activation: ReLU.
- Max Pooling Layer.
- Conv2D: 32 filters of size 3×3, stride 1 and padding 1.
- Activation: ReLU.
- Max Pooling Layer.
- Flattening Layer.
- Fully Connected Layer.
- Activation: ReLU.
- Output Layer: 4 output values representing x, y, width, height.

The CNN3 architecture is the following:

- Input Layer: The model accepts a single-channel image of dimensions 100×100 as input.
- Conv2D: 32 filters of size 3×3, with stride 1 and padding 1.
- Activation: ReLU.
- Max Pooling Layer.
- Conv2D: 40 filters of size 3×3, stride 1, and padding 1.
- Activation: ReLU.
- Max Pooling Layer.
- Conv2D: 48 filters of size 3×3, stride 1, and padding 1.
- Activation: ReLU.
- Flattening Layer.
- Fully Connected Layer.
- Activation: ReLU.
- Output Layer: 4 output values representing x, y, width, height.

7. Results and discussion

The derivatives of first and second order, in combination with binarization techniques, are employed in this experiment to preprocess data and extract representative features. The preprocessed data is considered as an input for the already described neural network models. The limit of epochs is set as 100. To regularize the model, such techniques as early stopping and restoring best weights are employed. Each of the neural network models is tested out without any preprocessing technique but normalization.

The following metrics are taken to measure the performance of the models: mean absolute error (MAE) and mean square error (MSE). Some of the most representative results are presented in Table 2.

Table 2
Metrics

Model	X		Y		Width		Height	
	MAE	MSE	MAE	MSE	MAE	MSE	MAE	MSE
CNN1 + Normalization	0.0491	0.0058	0.0567	0.0073	0.0542	0.0053	0.0631	0.0077
CNN1 + CD (1st order)	0.0201	0.0007	0.0165	0.0006	0.0224	0.0009	0.0213	0.0008
CNN1 + FD (1st order)	0.0142	0.0004	0.0164	0.0005	0.0206	0.0007	0.0223	0.0008
CNN1 + FD (2nd order)	0.0148	0.0004	0.0130	0.0004	0.0214	0.0007	0.0188	0.0006
CNN2 + Normalization	0.0200	0.0007	0.0225	0.0010	0.0279	0.0013	0.0351	0.0021
CNN2 + FD (2nd order)	0.0078	0.0001	0.0098	0.0002	0.0143	0.0004	0.0127	0.0003
CNN3 + Normalization	0.0189	0.0006	0.0197	0.0007	0.0257	0.0011	0.0305	0.0016
CNN3 + FD (1st order)	0.0073	0.0001	0.0080	0.0001	0.0153	0.0004	0.0128	0.0003
CNN3 + FD (2nd order)	0.0062	0.0001	0.0067	0.0001	0.0108	0.0002	0.0088	0.0001
CNN3 + FD (2nd order) + Binarization	0.0089	0.0001	0.0130	0.0003	0.0176	0.0005	0.0141	0.0003

Analyzing them there are next findings.

1. CNN with just normalization showed the worst results. Basically, preprocessing improves metrics by 2-4 times considering the same neural network architecture.
2. The combination of forward, central and backward derivatives of both the first and second derivatives showed quite a close impact on the performance. In some specific cases, forward differences outperformed it by around 10%. It is clearly shown for CNN with 3 convolution layers. However, considering the metrics for both CNN with 1 and 2 convolution layers, the difference is quite inconsistent. It might be stated that using both preprocessing techniques at the same time makes sense for future research. Thus, it means that the neural network architecture might be modified to be multi-channel in terms of input.
3. As for the previous point, using second-order or first-order derivatives had an impact mostly visible for CNN with 3 layers. The increase in performance, generally, does not exceed 10%.
4. Using binarization didn't have a positive impact on the metrics. It might require a better threshold-setting method than using just the meaning of the image. The method is not noise-resistance. We are speaking about the data that, in real-world scenarios, will be obtained by an IR scanner. Thus, the noise as Gaussian or similar will be present and binarization might provide many false contours as a result.

The following improvements and future research aspects are listed below.

1. Considering the specific nature of the INBEM method, the accuracy of potential calculation at the edges of the inclusion might be low. The parameters of INBEM, considering the scope of the paper, were looked up empirically and presented in the paper. The execution time was the main goal. The analysis showed quite moderate accuracy in specific cases, mainly with

the large inclusion. Thus, fine-tuning as an optimization task might be successfully done by a genetic algorithm (GA) or different techniques.

2. Considering the improvements in accuracy by using all the derivatives-based methods, it makes sense to use them for future investigation. It might make sense to use multi-channel input to combine all the positive aspects of the methods. At the same time, the idea of building ensembles of the models is worth considering.
3. The future research should include evaluating the already mentioned preprocessing methods with noisy data. Denoising methods should be considered too.
4. As the future aims to process real-world data, which are quite noisy, the preferred architecture for the model will be relying on CNN with 3 or more layers, as it is not just more accurate but extracts low-order features.

8. Conclusions

The results presented in the paper proved that INBEM, in combination with data preprocessing methods and neural networks, can solve the task of recognizing inclusion parameters. The numerical results showed that using second-order derivative preprocessing improved the prediction accuracy of geometric parameters by up to four times. The CNN3+FD (2nd-order) model showed the best performance, achieving a mean absolute error of less than 0.01, while CNN3+Normalization showed a mean absolute error between 0.019 and 0.03. It showed the perspective of using this combination of methods for estimating specifically the geometric parameters. Using such methods looks promising in terms of future research, aiming to be able to recognize multiple inclusions in 2D and 3D dimensions. As is stated, using INBEM as a tool for numerical experiments makes it feasible to produce large datasets in a reasonable time. Thus, it allows exploring new techniques and models of inclusion detection, preserving a wide variety of parameters of inclusions and the object.

The proposed approach, however, has certain limitations. It demonstrated lower accuracy of INBEM in corner regions. Thus, fine-tuning and regularization techniques look promising as a solution and must be considered in advance. The neural network model was validated only for stationary (steady-state) heat conduction and was not tested for transient (non-stationary) processes. In addition, the method is not yet noise-robust and requires further improvement in this direction. Also, the method was validated only for one inclusion detection task.

Thus, future research will aim to overcome these limitations, to extend the method towards recognizing multiple inclusions, and to perform simulation and detection in 3D space. Another important direction will be improving the robustness of the method when applied to noisy and real-world data, as real experiments typically introduce significant measurement noise. In addition, adapting the method for transient (non-stationary) heat conduction processes will also be considered, as this would expand its practical applicability in various industrial and scientific domains.

Declaration on Generative AI

The author(s) have not employed any Generative AI tools.

References

[1] C. M. Pimpalkhare, D. N. Pawaskar, Autonomous crack detection using deep learning on synthetic thermogram datasets, 2024.. arXiv:2412.16499.

[2] B. Szymanik, An evaluation of 3d-printed materials' structural properties using active infrared thermography and deep neural networks trained on the numerical data, Materials 15 (2022).

[3] L. Cheng, Z. Tong, S. Xie, M. Kersemans, Irt-gan: A generative adversarial network with a multi-headed fusion strategy for automated defect detection in composites using infrared thermography, Composite Structures 290 (2022) 115543. doi:10.1016/j.compstruct.2022.115543.

[4] W. F. Da Silva, R. A. C. Melo, M. Grosso, G. R. Pereira, D. B. Riffel, Active thermography data-processing algorithm for nondestructive testing of materials, IEEE Access 8 (2020) 175054–175062. doi:10.1109/ACCESS.2020.3025329.
[5] E. C. de Santana, W. F. da Silva, M. Grosso Lima, G. Ribeiro Pereira, D. B. Riffel, Three-dimensional printed subsurface defect detection by active thermography data-processing algorithm, 3D Printing and Additive Manufacturing 10 (2023) 420–427. doi:10.1089/3dp.2021.0172.
[6] Q. Fang, C. Ibarra-Castanedo, I. Garrido, Y. Duan, X. Maldague, Automatic detection and identification of defects by deep learning algorithms from pulsed thermography data, Sensors 23 (2023). doi:10.3390/s23094444.
[7] J. Hu, W. Xu, B. Gao, G. Y. Tian, Y. Wang, Y. Wu, Y. Yin, J. Chen, Pattern deep region learning for crack detection in thermography diagnosis system, Metals 8 (2018). doi:10.3390/met8080612.
[8] Y. Liu, F. Wang, Z. Jiang, S. Sfarra, K. Liu, Y. Yao, Generative deep learning-based thermographic inspection of artwork, Sensors 23 (2023). doi:10.3390/s23146362.
[9] L. M. Zhuravchak, N. V. Zabrods'ka, Solving of elastic dynamical problem in a porous fluid-saturated piecewise-homogeneous half-space by the indirect method of near-boundary elements, Radio Electronics, Computer Science, Control (2018) 40–48.
[10] Y. Turkan, J. Hong, S. Laflamme, N. Puri, Adaptive wavelet neural network for terrestrial laser scanner-based crack detection, Automation in Construction 94 (2018) 191–202.
[11] S. Teng, Z. Liu, G. Chen, L. Cheng, Concrete crack detection based on well-known feature extractor model and the yolo$v2network$, $AppliedSciences$11(2021). doi:10.3390/app11020813.
[12] T. Herrmann, C. Migniot, O. Aubreton, Cracks detection on glass object based on active thermography approach, in: C. Cudel, S. Bazeille, N. Verrier (Eds.), Fourteenth International Conference on Quality Control by Artificial Vision, volume 11172, International Society for Optics and Photonics, SPIE, 2019, p. 111721E. doi:10.1117/12.2520920.
[13] I. Garrido, J. Erazo-Aux, S. Lagüela, S. Sfarra, C. Ibarra-Castanedo, E. Pivarčiová, G. Gargiulo, X. Maldague, P. Arias, Introduction of deep learning in thermographic monitoring of cultural heritage and improvement by automatic thermogram pre-processing algorithms, Sensors 21 (2021). doi:10.3390/s21030750.
[14] J. Yang, W. Wang, G. Lin, Q. Li, Y. Sun, Y. Sun, Infrared thermal imaging-based crack detection using deep learning, IEEE Access 7 (2019) 182060–182077. doi:10.1109/ACCESS.2019.2958264.
[15] M. Rodríguez-Martín, J. G. Fueyo, D. Gonzalez-Aguilera, F. J. Madruga, R. García-Martín, L. Muñóz, J. Pisonero, Predictive models for the characterization of internal defects in additive materials from active thermography sequences supported by machine learning methods, Sensors 20 (2020). URL: https://www.mdpi.com/1424-8220/20/14/3982. doi:10.3390/s20143982.
[16] T. Leontiou, A. Frixou, M. Charalambides, E. Stiliaris, C. N. Papanicolas, S. Nikolaidou, A. Papadakis, Three-dimensional thermal tomography with physics-informed neural networks, Tomography 10 (2024)1930–1946. doi:10.3390/tomography10120140.
[17] L. M. Zhuravchak, Potential field modeling by combination of near-boundary and contact elements with non-classical finite differences in a heterogeneous medium, Mathematical Modeling and Computing 11 (2024) 373–384. doi:10.23939/mmc2024.02.373.
[18] L. Zhuravchak, N. Zabrodska, Algorithm for determining inclusion parameters in solving inverse problems of geoelectrical exploration using the profiling method, Geodynamics 1(36) (2024) 98–107. doi:10.23939/jgd2024.01.098.
[19] X.-Y. Gong, H. Su, D. Xu, Z.-T. Zhang, F. Shen, H.-B. Yang, An overview of contour detection approaches, International Journal of Automation and Computing 15 (2018) 656–672.
[20] D. L. Balageas, J.-M. Roche, F.-H. Leroy, W.-M. Liu, A. M. Gorbach, The thermographic signal reconstruction method: A powerful tool for the enhancement of transient thermographic images, Biocybernetics and Biomedical Engineering 35 (2015) 1–9. doi: 10.1016/j.bbe.2014.07.002.
[21] X. Guanxiang, V. Kovtun, The model of the system for objects recognition in the real-time video stream, Computer systems and information technologies (2024) 157–162. URL: https://csitjournal.khmnu.edu.ua/index.php/csit/article/view/362. doi:10.31891/csit- 2024- 4- 19.